Stopping and image forces on a charged particle moving parallel to an anisotropic two-dimensional material

Milad Moshayedi [1,*], Maria Rosa Preciado Rivas [1,†] and Zoran L. Mišković [2,‡]

[1]*Department of Applied Mathematics, University of Waterloo, Waterloo, Ontario, Canada, N2L 3G1*
[2]*Department of Applied Mathematics and Waterloo Institute for Nanotechnology, University of Waterloo,*
Waterloo, Ontario, Canada, N2L 3G1

We use a classical dielectric response framework to evaluate the force components acting on a point charge that moves parallel to an anisotropic two-dimensional material representing doped phosphorene. The anisotropic response of phosphorene is captured by a simple analytical conductivity model that combines contributions from its inter- and intraband electronic transitions, thereby giving rise to a topological transition between elliptic and hyperbolic isofrequency curves for its plasmon modes in the terahertz to the midinfrared frequency range. Pairing this model with a simple dielectric description of a SiO$_2$ substrate further reveals the effects of plasmon hybridization with optical phonons in the substrate. We have found that the force on the incident charge has three components, which all exhibit strong velocity-dependent anisotropy when its direction of motion is varied with respect to the principal directions of the phosphorene's conductivity tensor. Besides the longitudinal stopping force and the dynamic image force, there arises a transverse stopping force, with a magnitude comparable to that of the longitudinal force, which acts parallel to the target surface and perpendicular to the trajectory of the particle, and can be therefore experimentally observable, even after its magnitude is reduced by the presence of the substrate. In addition, we have found that the dynamic image force can become repulsive when the particle moves along the armchair direction of a freestanding phosphorene, but the presence of the substrate eliminates that surprising but implausible consequence of the adopted model for anisotropic conductivity of that material.

I. INTRODUCTION

Black phosphorus (BP) is considered "a rising star 2D nanomaterial in the post-graphene era" [1], which holds strong promise for optoelectronic applications because of its pronounced in-plane anisotropy, making this material substantially different from the broad class of uniaxial crystals [2–7]. Namely, the elementary building block of BP, called phosphorene, is a monoatomic 2D material in the form of a puckered honeycomb-structured monolayer which exhibits large variations in its mechanical, electrical, and optical properties, when probed along its principal crystalline axes, labeled as the armchair (AC) and the zigzag (ZZ) directions [4,8,9]. With its electronic band structure of a 2D direct-gap semiconductor, exhibiting strongly anisotropic in-plane conductivity, phosphorene has been long considered a promising candidate for a naturally occurring hyperbolic metasurface [6,10]. Such surfaces can host the so-called hyperbolic plasmon polariton modes characterized by hyperbolic isofrequency dispersion curves, which imply strong directionality of their in-plane propagation that is accompanied by relatively large wave numbers, thereby making hyperbolic metasurfaces interesting for applications, e.g., in wave guiding, hyperlensing,

and negative refraction [11]. Naturally occurring hyperbolic metasurfaces based on anisotropic 2D materials, such as phosphorene, are also technologically advantageous for device applications because of their ease of fabrication and the dynamic tunability of their optical response [6,12,13].

The tunability of the optical response of BP has been studied theoretically in great detail in terms of changeable layer thickness, mechanical strain, doping density and the nearby dielectrics [14–18]. The tunability of hyperbolic plasmon polariton modes in BP was recently demonstrated experimentally in the midinfrared (MIR) frequency range by controlling the intraband electronic transitions via changing the doping density in phosphorene layers, which was achieved by an externally applied gate potential through a stack consisting of BP, hexagonal boron-nitride (hBN) cladding layers and a SiO$_2$ substrate [19,20]. Moreover, tuning the density of quasifree charge carriers in phosphorene was predicted theoretically to give rise to plasmon polariton modes that exhibit a topological transition between elliptic and hyperbolic isofrequency dispersion curves, which typically take place in the terahertz (THz) and the MIR frequency ranges, respectively [21–24]. A significant progress was achieved in theoretical modeling of the optical anisotropy of doped phosphorene by means of an in-plane conductivity tensor [15,23], which was used to demonstrate a relation between the tunability and the directionality effects in launching the elliptic and hyperbolic plasmons, induced by a nearby stationary radiating dipole with adjustable polarization [22,25–27]. Besides the extensive

*mmoshaye@uwaterloo.ca
†mrprecia@uwaterloo.ca
‡zmiskovi@uwaterloo.ca

use of analytical models for the optical conductivity of doped phosphorene in the technologically important THz-MIR frequency range [15,22,23,25–28], there are several *ab initio* calculations of that conductivity, which cover a much broader range of frequencies, from the THz to the vacuum ultraviolet [29–32].

In addition to using polarization-resolved optical spectroscopies and localized probes in the form a radiating dipole source, which can only explore plasmon polaritons in nanostructures at a fixed frequency, there is increasing interest in using interactions with external charged particles to examine optical response of 2D materials over a broad range of frequencies and wave vectors [33,34]. In that respect, particularly sensitive to the low-energy surface excitations are the vibrational and valence aloof beam electron energy loss spectroscopy (EELS) in a monochromated scanning transmission electron microscope (STEM) [35–38], high-resolution EELS (HREELS) using low-energy electron reflection from surfaces [39–44], and grazing scattering of medium-energy ions from surfaces [45–50]. In particular, the momentum-resolved HREELS experiments proved to be quite successful in revealing the tunability of the sheet plasmon (sometimes also called the Dirac plasmon) in doped graphene and its hybridization with optical phonon modes in an insulating polar substrate, which takes place in the THz-MIR range of frequency [44,51–57]. It is therefore tempting to contemplate that a similar type of experiment should also be effective in probing the directionality in exciting the elliptic and hyperbolic plasmon modes in doped phosphorene by incident charged particles. Based on our theoretical work on graphene [58], the effects of the incident particle trajectory are most pronounced for near-grazing scattering angles, which was also well documented to be the most surface-sensitive regime in HREELS and ion-surface scattering experiments [40,49].

The experiments using a charged particle moving on an aloof trajectory or under grazing incidence upon the target surface can be modeled by assuming that the particle moves parallel to the surface at fixed velocity, whereas its motion perpendicularly to the surface may be treated as adiabatically slow on a time scale of the target response [48]. When such particle moves over the surface of an isotropic material, there are two types of forces that affect its trajectory: a dissipative force, called the stopping force, which is parallel to the surface and acts in the direction of particle's motion causing its slowing down, and a conservative force, or the dynamic image force, which is perpendicular to the surface and is necessarily attractive [59], causing the bending of particle's trajectory to the surface [40,46,48]. It is therefore interesting to explore the nature of those two types of forces when charged particle moves over the surface of an anisotropic 2D material. In that context, it is worth mentioning that theoretical studies of the stopping force on fast charged particles traversing slabs of uniaxial crystals, such as highly oriented pyrolytic graphite [60] or hBN [61], predicted strong directional effects in that force due to anisotropy in the dielectric response of those materials. Based on the conclusions of those two studies of anisotropic 3D materials, one may expect that the stopping force on a charge moving parallel to an anisotropic 2D material, such as phosphorene, will still be parallel to its surface, but having two components that act in the direction of the

particle's motion and perpendicular to it, which we shall call the *longitudinal* and *transverse* stopping forces, respectively. On the other hand, it is difficult to envisage the nature of the dynamic image force on a particle moving over the surface of an anisotropic 2D material without even posing a fundamental question whether such a force should be *a priori* attractive for all directions of its motion [62].

In this paper, we address those questions by adopting classical description of the total force on a charged particle moving parallel to a general anisotropic 2D material, with its electrodynamic polarization described by a dielectric response formalism within the nonretarded approximation. We limit our focus to the THz-MIR frequency range for doped phosphorene, exhibiting a topological transition between the elliptic and hyperbolic plasmon dispersions, which are expected to be efficiently probed by a particle moving at a speed on the order of several Bohr velocities, pertaining to the HREELS or ion-surface grazing scattering techniques [40,46]. We find that the longitudinal and transverse stopping forces, as well as the image force on such a particle indeed exhibit strong anisotropy when the direction of particle's motion varies with respect to the principal directions of phosphorene, as a direct consequence of the anisotropy of its plasmon modes. In particular, we find that the transverse stopping force, which vanishes above an isotropic surface, tends to bend the particle's trajectory toward the AC direction of phosphorene at lower speeds and it bends it toward the ZZ direction at higher speeds. Moreover, we find that the image force is mostly attractive, as expected, but can become repulsive for a particle moving in a direction close to the AC direction of freestanding phosphorene at higher speeds. We discuss this unexpected and counterintuitive result and trace it to an insufficiency of the anisotropic Drude model for conductivity at high frequencies, which could be remedied by the inclusion of a full contribution from the interband electron transitions in phosphorene. Notwithstanding the limitations of our conductivity modeling, we suggest that the effects of anisotropy, especially the occurrence of the transverse stopping force, should be observable, e.g., in a momentum-resolved HREELS experiment with grazingly incident electrons.

In the following section, we first describe a simple model for the optical conductivity tensor of doped phosphorene in the THz-MIR frequency range and use it to compute all three force components for both freestanding phosphorene and in the presence of transverse optical phonons in a SiO_2 substrate. The presentation and the discussion of the results is followed by our concluding remarks. Unless stated otherwise, we shall use Gaussian units of electrostatics.

II. THEORY

In order to make our analytical modeling of the dielectric response of phosphorene feasible, we focus our attention to particles that move at large distances above it, in excess of a nanometer, and at the speeds in excess of the Bohr velocity. While the restriction to large distances does not allow for a complete modeling of a HREELS experiment, it enables us to formulate an effective 2D dielectric function by invoking the so-called optical limit for the in-plane conductivity of

doped phosphorene, which neglects its nonlocal, i.e., spatially dispersive features.

We use a Cartesian system with coordinates $(\mathbf{r}, z)$, where $\mathbf{r} = (x, y)$, and assume that a 2D anisotropic material is represented by a conductive sheet with zero thickness and large area, which is placed in the $z = 0$ plane, a semi-infinite substrate occupies the region $z \leqslant -d$ below graphene, while the regions $-d < z < 0$ and $z > 0$ are vacuum [63]. The electrodynamic response of this system can be described in a nonretarded regime by solving the Poisson equation, which is greatly simplified by performing a 2D Fourier transform with respect to the position, $\mathbf{r} \to \mathbf{q}$, where $\mathbf{q} = (q_x, q_y)$, and time, $t \to \omega$. As discussed elsewhere [64], the Poisson equation can be then easily solved, while taking account of the conductive sheet by means of a boundary condition at $z = 0$ for the total electric field, which is supplemented by a relation between the areal density of charge induced on that sheet, $\widetilde{\rho}_{2D}(\mathbf{q}, \omega)$, and the value of the total electrostatic potential, $\widetilde{\Phi}^0(\mathbf{q}, \omega)$, evaluated in the plane $z = 0$.

A. Modeling dielectric response of phosphorene in the THz–MIR range

In the linear regime of a random phase approximation (RPA), we may write in the Fourier domain $\widetilde{\rho}_{2D}(\mathbf{q}, \omega) = -e^2 \chi(\mathbf{q}, \omega)\widetilde{\Phi}^0(\mathbf{q}, \omega)$, where $\chi(\mathbf{q}, \omega)$ is a density response function for the longitudinal polarization of noninteracting electrons in a 2D material. In order to reveal the anisotropy of that material, it is convenient to express that function in terms of the in-plane conductivity tensor, $\overleftrightarrow{\sigma}(\mathbf{q}, \omega)$, which may be accomplished by referring to the in-plane Ohm's law, $\widetilde{\mathbf{J}}_{2D}(\mathbf{q}, \omega) = \overleftrightarrow{\sigma}(\mathbf{q}, \omega) \cdot \widetilde{\mathbf{E}}^0_\parallel(\mathbf{q}, \omega)$, where $\widetilde{\mathbf{J}}_{2D}(\mathbf{q}, \omega)$ is the in-plane charge current, induced in the 2D material, and $\widetilde{\mathbf{E}}^0_\parallel(\mathbf{q}, \omega) = -i\mathbf{q}\,\widetilde{\Phi}^0(\mathbf{q}, \omega)$ is the tangential component of the total electric field, evaluated at $z = 0$. Combining the above three relations with the in-plane charge continuity equation, $\omega \widetilde{\rho}_{2D}(\mathbf{q}, \omega) = \mathbf{q} \cdot \widetilde{\mathbf{J}}_{2D}(\mathbf{q}, \omega)$, finally gives

$$\chi(\mathbf{q}, \omega) = \frac{i}{e^2 \omega} \mathbf{q} \cdot \overleftrightarrow{\sigma}(\mathbf{q}, \omega) \cdot \mathbf{q}. \quad (1)$$

We are interested in the optical limit of the polarization of the 2D material, which is achieved by setting $\mathbf{q} \to \mathbf{0}$ in $\overleftrightarrow{\sigma}(\mathbf{q}, \omega)$ [65], rendering the conductivity tensor diagonal in a Cartesian coordinate system, with its x and y components being functions of frequency only, $\sigma_x(\omega)$ and $\sigma_y(\omega)$. Then, the density response function becomes

$$\chi(\mathbf{q}, \omega) = \frac{i}{e^2 \omega}\big[q_x^2 \sigma_x(\omega) + q_y^2 \sigma_y(\omega)\big], \quad (2)$$

which may be more conveniently written by switching to polar coordinates for the wavevector, $\mathbf{q} = (q, \theta)$, as $\chi(q, \theta, \omega) = i\frac{q^2}{e^2 \omega}\sigma(\theta, \omega)$, where $q = \sqrt{q_x^2 + q_y^2}$ and the angle-dependent optical conductivity is defined by

$$\sigma(\theta, \omega) = \sigma_x(\omega)\cos^2\theta + \sigma_y(\omega)\sin^2\theta. \quad (3)$$

We note that $\sigma(\theta, \omega)$ is the longitudinal component of a full conductivity tensor in doped phosphorene [66,67], in which case the Cartesian x and y axes may be taken along its AC and ZZ directions, respectively, so that the polar angle θ is taken with respect to the AC direction. With the in-plane Coulomb

interaction potential given by $V_C(q) = 2\pi e^2/q$, we may express an effective 2D dielectric function of a freestanding 2D material with $d \to \infty$ as

$$\epsilon_{2D}(\mathbf{q}, \omega) = 1 + V_C(q)\chi(\mathbf{q}, \omega) = 1 + i2\pi\frac{q}{\omega}\sigma(\theta, \omega). \quad (4)$$

Both components of the optical conductivity tensor are generally decomposed within the RPA into the intraband and interband contributions [32,68], $\sigma_j(\omega) = \sigma_j^{\text{intra}}(\omega) + \sigma_j^{\text{inter}}(\omega)$ for $j = x, y$. We wish to develop a phenomenological model for the optical conductivity tensor of doped phosphorene that will be useful at low frequencies covering the technologically relevant THz-MIR range of frequencies. In that range, the intraband conductivity should be adequately represented by an anisotropic Drude model [15,19,20,32]:

$$\sigma_j^{\text{intra}}(\omega) = \frac{i}{\pi}\frac{D_j}{\omega + i\gamma_j}, \quad (5)$$

where the Drude weight, D_j, may be expressed at zero temperature in terms of the equilibrium doping density n and an effective electron or hole mass m_j^* as $D_j = \pi e^2 |n|/m_j^*$ for the direction $j = x, y$. The damping rate $\gamma_j = 1/\tau_j$ in Eq. (5) is allowed to depend on the direction as well, and it may be expressed in terms of the mobility tensor of phosphorene having Cartesian components μ_j. By using a relation involving the dc conductivity tensor, $\sigma_j^{\text{intra}}(0) = e|n|\mu_j$, we may write $\tau_j = \mu_j m_j^*/e$ for $j = x, y$.

On the other hand, for a 2D semiconductor with the band gap energy ε_g, the real part of its interband conductivity, $\Re[\sigma_j^{\text{inter}}(\omega)]$, is negligible at frequencies $0 < \omega \lesssim \omega_g$, where $\omega_g = \varepsilon_g/\hbar$. Therefore, because $\varepsilon_g \approx 2$ eV for phosphorene, in order to take into account the interband contribution to its optical conductivity at the THz-MIR frequencies, for which $\omega \ll \omega_g$, it is sufficient to find an approximation for the imaginary part of the interband conductivity, $\Im[\sigma_j^{\text{inter}}(\omega)]$, in the limit $\omega \to 0$. The *ab initio* data show that quite generally for a 2D material [32,65], $\Im[\sigma_j^{\text{inter}}(\omega)]$ behaves as linear function when $\omega \to 0$, having a negative slope, say $-\alpha_j$. Accordingly, we can approximate the interband conductivity of doped phosphorene in the THz-MIR frequency range by using $\sigma_j^{\text{inter}}(\omega) \approx -i\alpha_j\omega$ for $j = x, y$, where $\alpha_j > 0$ may be regarded as the Cartesian components of its in-plane polarizability tensor in the static limit, which arise from high-energy interband electronic transitions. It is expected that the values of α_j are rather independent from the doping density for sufficiently small values of $|n|$, which was confirmed by *ab initio* calculations for phosphorene.

One may determine the numerical values of α_j in two ways by using *ab initio* data for $\sigma_j^{\text{inter}}(\omega)$. First, α_j can be evaluated as the slope of the imaginary part of the interband optical conductivity at vanishing frequency,

$$\alpha_j = -\lim_{\omega \to 0}\frac{1}{\omega}\Im[\sigma_j^{\text{inter}}(\omega)]. \quad (6)$$

An alternate method for determining α_j can be deduced from a Kramers-Kronig relation between the real and imaginary parts of $\sigma_j^{\text{inter}}(\omega)$,

$$\Im[\sigma_j^{\text{inter}}(\omega)] = -\frac{2}{\pi}\omega\mathcal{P}\int_0^\infty \frac{d\omega'}{(\omega')^2 - \omega^2}\Re[\sigma_j^{\text{inter}}(\omega')], \quad (7)$$

where $\mathcal{P}$ indicates a Cauchy principal value type of the integral over ω'. Therefore, referring to Eqs. (6) and (7), α_j may be computed from *ab initio* data for the real part of the interband optical conductivity as an integral in the form of a sum rule for each direction $j = x, y$,

$$\alpha_j = \frac{2}{\pi} \int_0^\infty \frac{d\omega}{\omega^2} \Re[\sigma_j^{\text{inter}}(\omega)]. \quad (8)$$

A similar phenomenological treatment of high-energy interband electronic transitions was recently proposed by Gjerding *et al.* [69] in order to expand the domain of applicability of the Dirac model for conductivity of doped graphene. Moreover, a minimal analytical model for conductivity of doped phosphorene, proposed by Nemilentsau *et al.* [23], contains steplike terms in $\Re[\sigma_j^{\text{inter}}(\omega)]$, which give rise to similar contributions of interband transitions in the gap region of frequencies as in the present model. As discussed in Ref. [23], the presence of $\Im[\sigma_j^{\text{inter}}(\omega)]$ in the THz-MIR frequency range, when combined with the anisotropic Drude model (5) for intraband transitions, is essential for the occurrence of hyperbolic isofrequency dispersion curves in the (q_x, q_y) plane, which requires that the imaginary parts of the x and y components of the total conductivity have the opposite signs [11,18,23].

Finally, the effective 2D dielectric function for doped free-standing phosphorene may be approximated in the THz-MIR frequency range as follows:

$$\epsilon_{2D}(q_x, q_y, \omega) = 1 + i\frac{2\pi}{q\omega}\left[q_x^2 \sigma_x(\omega) + q_y^2 \sigma_y(\omega)\right] \quad (9)$$

$$\approx 1 + \frac{2\pi}{q}\left(\alpha_x q_x^2 + \alpha_y q_y^2\right)$$

$$- \frac{2}{q\omega}\left(\frac{D_x q_x^2}{\omega + i\gamma_x} + \frac{D_y q_y^2}{\omega + i\gamma_y}\right), \quad (10)$$

which constitutes what we call the *optical model* of the dynamic polarization of phosphorene. A similar version of an isotropic model was shown to work extremely well for graphene doped with the Fermi energy of 200 meV in comparison with *ab initio* data in a range of small wave numbers, $q \lesssim 0.1$ nm^{-1} [68]. Solving the equation $\epsilon_{2D}(q_x, q_y, \omega) = 0$ in the limit when both γ_x and γ_y vanish immediately yields a dispersion relation for anisotropic plasmon modes in doped phosphorene as $\omega = \omega_p(q_x, q_y)$, with

$$\omega_p(q_x, q_y) = \sqrt{2\frac{D_x q_x^2 + D_y q_y^2}{q + a_x q_x^2 + a_y q_y^2}}, \quad (11)$$

where $a_j = 2\pi\alpha_j$ for $j = x, y$. The above expression shows that the inclusion of the interband correction into our optical model causes the plasmon frequency to level off at a nondispersing, but direction-dependent frequency in the interval $\omega_{h1} < \omega < \omega_{h2}$, where $\omega_{h1,2} = \text{min,max}(\sqrt{\frac{D_x}{\pi\alpha_x}}, \sqrt{\frac{D_y}{\pi\alpha_y}})$ when the wave number q exceeds $\sim 1/\text{min}(a_x, a_y) \approx 0.3$ nm^{-1} (see below for the adopted parameters). This fact calls for an estimate of the nonlocal effects in the dielectric response of doped phosphorene, which is done in Sec. S2 of Ref. [70] using the Boltzmann equation for the intraband electron transitions in an anisotropic material [63,71–75]. Combining that result

with the present interband correction gives rise to what we call a *semiclassical model*, see Eq. (S8) in Ref. [70], which exposes nonlocal effects to the leading order in q when compared with the optical model. However, it is shown in Sec. S3 of Ref. [70] that nonlocal effects in the plasmon dispersion and in all three forces are negligible for the present choice of the particle distances and speeds. Accordingly, we choose the optical model developed in this section to present our results for forces, later in Sec. III B.

B. Force on the moving charge

We assume that an external point charge Ze moves at fixed distance $z_0 > 0$, parallel to an anisotropic 2D layer with the conductivity tensor $\overleftrightarrow{\sigma}(\mathbf{q}, \omega)$. The particle's velocity $\mathbf{v} = (v_x, v_y)$ is assumed to be constant, so that its charge density is $\rho_{\text{ext}}(\mathbf{r}, z, t) = Ze\,\delta(\mathbf{r} - \mathbf{v}t)\,\delta(z - z_0)$. The direction of the velocity is defined by an angle θ_0 with respect to the x axis, so that $v_x = v\cos\theta_0$ and $v_y = v\sin\theta_0$ with v being the speed. Following Refs. [54,76], the Fourier transform of the induced potential in the region $z > 0$, may be expressed in the presence of an isotropic substrate with dielectric permittivity $\epsilon_s(\omega)$ underneath the 2D layer as

$$\widetilde{\Phi}_{\text{ind}}^>(\mathbf{q}, z, \omega) = \left[\frac{1}{\epsilon_{2D}(\mathbf{q}, \omega)} - 1\right]\widetilde{\Phi}_{\text{ext}}^0(\mathbf{q}, \omega)\,e^{-qz}, \quad (12)$$

where

$$\epsilon_{2D}(\mathbf{q}, \omega) = \epsilon_{\text{bg}}(q, \omega) + i\frac{2\pi}{q\omega}\mathbf{q} \cdot \overleftrightarrow{\sigma}(\mathbf{q}, \omega) \cdot \mathbf{q} \quad (13)$$

is an effective 2D dielectric function of the combined layer-substrate system, with the background dielectric function defined as

$$\epsilon_{\text{bg}}(q, \omega) = \left[1 - \frac{\epsilon_s(\omega) - 1}{\epsilon_s(\omega) + 1}\,e^{-2qd}\right]^{-1} \quad (14)$$

and

$$\widetilde{\Phi}_{\text{ext}}^0(\mathbf{q}, \omega) = 2\pi Ze\,\delta(\omega - \mathbf{q}\cdot\mathbf{v})\frac{2\pi}{q}e^{-qz_0} \quad (15)$$

is the value of the Fourier transform of the potential due to the external charged particle, taken at $z = 0$.

The total force on the particle is evaluated from the space and time dependent expression for the induced electric field upon substitution $\mathbf{r} = \mathbf{v}t$ and $z = z_0$ as $\mathbf{F} = Ze\mathbf{E}_{\text{ind}}(\mathbf{v}t, z_0, t)$, where

$$\mathbf{E}_{\text{ind}}(\mathbf{r}, z, t) = -\left(\frac{\partial}{\partial\mathbf{r}} + \hat{\mathbf{z}}\frac{\partial}{\partial z}\right)\Phi_{\text{ind}}^>(\mathbf{r}, z, t)$$

$$= -\iint \frac{d^2\mathbf{q}}{(2\pi)^2}\int_{-\infty}^{\infty}\frac{d\omega}{2\pi}\,e^{i(\mathbf{q}\cdot\mathbf{r} - \omega t)}$$

$$\times \left(i\mathbf{q} + \hat{\mathbf{z}}\frac{\partial}{\partial z}\right)\widetilde{\Phi}_{\text{ind}}^>(\mathbf{q}, z, \omega), \quad (16)$$

with $\widetilde{\Phi}_{\text{ind}}^>(\mathbf{q}, z, \omega)$ given in Eq. (12). Taking into account the symmetry property of the effective 2D dielectric function $\epsilon_{2D}(-\mathbf{q}, -\omega) = \epsilon_{2D}^*(\mathbf{q}, \omega)$, the total force is decomposed into parallel and perpendicular components according to $\mathbf{F} = \mathbf{F}_\parallel + \hat{\mathbf{z}}F_i$,

where

$$\mathbf{F}_{\parallel} = \frac{(Ze)^2}{2\pi} \iint d^2\mathbf{q}\, e^{-2qz_0}\, \hat{\mathbf{q}}\, \Im\left[\frac{1}{\epsilon_{2D}(\mathbf{q}, \mathbf{q}\cdot\mathbf{v})}\right], \quad (17)$$

is the stopping force with $\hat{\mathbf{q}} = \mathbf{q}/q$, and

$$F_i = \frac{(Ze)^2}{2\pi} \iint d^2\mathbf{q}\, e^{-2qz_0}\, \Re\left[\frac{1}{\epsilon_{2D}(\mathbf{q}, \mathbf{q}\cdot\mathbf{v})} - 1\right] \quad (18)$$

is the image force. Notice that the designation of the above forces into stopping and image forces stems from the fact that they are expressed in terms of the imaginary and real parts of the inverse of the 2D permittivity $\epsilon_{2D}(\mathbf{q}, \omega)$, respectively [59]. It is quite crucial for the emergence of directionality effects in the above forces that the frequency in the 2D permittivity in Eqs. (17) and (18) is substituted according to $\omega = \mathbf{q}\cdot\mathbf{v} = v(q_x \cos\theta_0 + q_y \sin\theta_0)$, which stems from the Dirac delta function in Eq. (15), and expresses Galilean kinematic resonance between the layer's and particle's frames of reference.

It is physically revealing to further decompose the stopping force into a longitudinal component, F_ℓ, and transverse component, F_t, according to $\mathbf{F}_{\parallel} = \hat{\mathbf{v}}F_\ell + (\hat{\mathbf{z}} \times \hat{\mathbf{v}})F_t$, where $\hat{\mathbf{v}} = \mathbf{v}/v$ and $\hat{\mathbf{z}}$ is a unit vector in the direction of the z axis. Accordingly, we may write $\hat{\mathbf{q}} = \hat{\mathbf{v}}\cos(\theta-\theta_0) + (\hat{\mathbf{z}} \times \hat{\mathbf{v}})\sin(\theta-\theta_0)$ in Eq. (17) and switch to polar coordinates for integration over the wavevector $\mathbf{q} = (q, \theta)$ in both Eqs. (17) and (18), to finally express the three force components as

$$F_\ell = \frac{Z^2 e^2}{2\pi} \int_0^\infty dq\, q\, e^{-2qz_0}$$
$$\times \int_0^{2\pi} d\theta\, \cos(\theta-\theta_0)\, \Im\left[\frac{1}{\epsilon_{2D}(q, \theta, \mathbf{q}\cdot\mathbf{v})}\right], \quad (19)$$

$$F_t = \frac{Z^2 e^2}{2\pi} \int_0^\infty dq\, q\, e^{-2qz_0}$$
$$\times \int_0^{2\pi} d\theta\, \sin(\theta-\theta_0)\, \Im\left[\frac{1}{\epsilon_{2D}(q, \theta, \mathbf{q}\cdot\mathbf{v})}\right], \quad (20)$$

$$F_i = \frac{Z^2 e^2}{2\pi} \int_0^\infty dq\, q\, e^{-2qz_0}$$
$$\times \int_0^{2\pi} d\theta\, \Re\left[\frac{1}{\epsilon_{2D}(q, \theta, \mathbf{q}\cdot\mathbf{v})} - 1\right], \quad (21)$$

where the frequency to be substituted in the 2D dielectric permittivity $\epsilon_{2D}(q, \theta, \omega)$ is given by $\omega = \mathbf{q}\cdot\mathbf{v} = qv\cos(\theta-\theta_0)$. For our conductivity model of doped phosphorene in the optical limit, the polar form of the 2D permittivity may be written explicitly as

$$\epsilon_{2D}(q, \theta, \omega) = \epsilon_{bg}(q, \omega) + q(a_x \cos^2\theta + a_y \sin^2\theta)$$
$$- 2\frac{q}{\omega}D_0\left(\frac{1}{\overline{m}_x^*}\frac{\cos^2\theta}{\omega + i\gamma_x} + \frac{1}{\overline{m}_y^*}\frac{\sin^2\theta}{\omega + i\gamma_y}\right), \quad (22)$$

where $D_0 = \pi|n|/m_0$, whereas $\overline{m}_x^* = m_x^*/m_0$ and $\overline{m}_y^* = m_y^*/m_0$ are the reduced electron or hole effective masses with m_0 being the bare electron mass. With the polar angle defined with respect to the AC direction of phosphorene, which is adopted for the x axis, the symmetry properties of the 2D dielectric permittivity imply that all the force components in Eqs. (19)–(21) are periodic functions of the incidence angle

θ_0 with the period π, i.e., the force components do not change upon reversing the direction of motion. Moreover, the longitudinal stopping force and the image force are symmetric (even) functions of θ_0 with respect to the principal directions of phosphorene, $\theta_0 = 0$ (AC) and $\theta_0 = \pi/2$ (ZZ), whereas the transverse stopping force is an antisymmetric (odd) function with respect to the principal directions.

As for the substrate, we shall consider SiO$_2$, which exhibits two prominent transverse optical (TO) phonon modes at frequencies, ω_{TO1} and ω_{TO2}, with its bulk dielectric permittivity modeled by [76]

$$\epsilon_s(\omega) = \epsilon_\infty + (\epsilon_0 - \epsilon_i)\frac{\omega_{TO1}^2}{\omega_{TO1}^2 - \omega(\omega + i\gamma_{TO1})}$$
$$+ (\epsilon_i - \epsilon_\infty)\frac{\omega_{TO2}^2}{\omega_{TO2}^2 - \omega(\omega + i\gamma_{TO2})}, \quad (23)$$

where ϵ_0, ϵ_i and ϵ_∞ are the static, intermediate and infinite-frequency dielectric constants, and γ_{TO1} and γ_{TO2} the corresponding damping rates. In view of recent interest in using hBN in van der Waals heterostructures in combination with various 2D materials [27,77], we note that the present theory can be readily generalized to take into account the anisotropic nature of a 3D tensorial dielectric permittivity of a uniaxial substrate. However, with the c axis of such a material typically oriented along the z coordinate axis in our setting, there would be no substantially new effects regarding the in-plane anisotropy of phosphorene, so we limit our interest in this work to a substrate with isotropic permittivity, such as SiO$_2$.

III. DISCUSSION OF THE RESULTS

For the parameters pertaining to phosphorene, we used the numerically obtained *ab initio* data from Ref. [32] for the n doped case with the density of $n = 10^{13}$ cm^{-2}, giving a Fermi energy of 52.2 meV with respect to the bottom of the lowest-lying conduction band. Specifically, we adopted $\alpha_x = 0.572$ nm and $\alpha_y = 0.488$ nm for static polarizabilities due to interband transitions, whereas the reduced effective electron masses in the direction j were deduced from the *ab initio* data for "effective numbers of charge carriers" n_j^e, simply as $\overline{m}_x^* = n/n_x^e \approx 0.133$ and $\overline{m}_y^* = n/n_y^e \approx 1.119$. For an estimate of the mobility due to electron scattering on charged impurities, we adopted the values from Ref. [78], $\mu_x \approx 700$ cm^2 V^{-1} s^{-1} and $\mu_y \approx 113$ cm^2 V^{-1} s^{-1}, giving $\hbar\gamma_x \approx 12.4$ meV and $\hbar\gamma_y \approx 9.2$ meV, respectively. We note that the anisotropies in the static polarizabilities α_j and the damping rates γ_j are not particularly strong. We found in our calculations of the force components that the anisotropies in α_j and γ_j do not play as important a role as the anisotropy in the effective electron masses defining the Drude model.

The parameters to be used in the dielectric permittivity of the SiO$_2$ substrate in Eq. (23) are [76] $\epsilon_0 = 3.9$, $\epsilon_i = 3.05$ and $\epsilon_\infty = 2.5$; $\hbar\omega_{TO1} = 55.6$ meV and $\hbar\omega_{TO2} = 138.1$ meV; $\hbar\gamma_{TO1} = 5.37$ meV and $\hbar\gamma_{TO2} = 8.95$ meV. Note that, from these parameters, we obtain two Reststrahlen bands, occupying the frequency intervals $\omega_{TO1} < \omega < \omega_{SO1}$ and $\omega_{TO2} < \omega < \omega_{SO2}$, where $\hbar\omega_{SO1} \approx 60.9$ meV and $\hbar\omega_{SO2} \approx 146.5$ meV correspond to the frequencies of the

related Fuchs-Kliewer, or surface optical phonons in the SiO$_2$ substrate. For the size of the gap between phosphorene and the substrate. we take $d = 0.4$ nm as a representative value for a van der Waals distance.

The effects of speed of the incident charged particle will be discussed using its reduced form by normalizing it as $\bar{v} = v/v_B$, where $v_B = e^2/\hbar \approx c/137$ is the Bohr velocity.

A. Dispersion relations

We first discuss the dispersion relations for plasmon modes in doped phosphorene, which can be obtained by solving the equation $\epsilon_{2D}(q_x, q_y, \omega) = 0$ when all the damping parameters are set to zero. We compare the results obtained by using three models of increasing complexity: (a) anisotropic *Drude model* covering only the intraband electron transitions, (b) full *optical model*, consisting of the Drude model plus the interband correction to the conductivity introduced in the section II A, and (c) *semiclassical model*, which consists of a spatially dispersive polarization function for the intraband transitions from Sec. S2 of Ref. [70] plus the same interband correction as in the optical model.

In order to emphasize the key role of the interband contribution in our conductivity models, we first consider the case of a freestanding phosphorene layer ($d \to \infty$). We remark that, within the optical model, the isofrequency curves become open in the frequency interval $\omega_{h1} < \omega < \omega_{h2}$, where $\hbar\omega_{h1} = \hbar e \sqrt{\frac{n}{m_y^* \alpha_y}} \approx 142$ meV and $\hbar\omega_{h2} = \hbar e \sqrt{\frac{n}{m_x^* \alpha_x}} \approx 379$ meV are obtained from the above parameters for phosphorene, giving rise to hyperbolic modes in the MIR frequency range. However, the inclusion of the nonlocal effects via the semiclassical model prevents the plasmon frequency in Eq. (11) from crossing into the continuum of the intraband electron-hole (e-h) excitations at increasing wave numbers, as shown in Fig. S9 of Ref. [70]. The resulting isofrequency curves in the semiclassical model become then again closed, but they still exhibit quasihyperbolic shapes in the MIR range, which are similar to those in the optical model at small wave numbers. On the other hand, at frequencies in the THz range, phosphorene operates in the elliptic regime, or more appropriately quasielliptic regime, where the isofrequency dispersion is given by closed curves in the shape of an elongated numeral eight. [22,23] In that regime, the wave numbers are typically $\ll 1$ nm^{-1} making the roles of both the interband correction and nonlocal effects negligible, so that the anisotropic Drude model of doped phosphorene should suffice, although retardation effects may set in.

In order to exhibit a transition from the elliptic to hyperbolic regimes in freestanding phosphorene, we show in Fig. 1(a) the isofrequency curves from the dispersion surface $\omega = \omega_p(q_x, q_y)$ for $\hbar\omega = 50, 100, 150, 200$, and 250 meV using the Drude model (green curves), optical model (red curves) and semiclassical model (blue curves, see Eq. (S10) in Ref. [70]). One can verify that the two innermost curves for 50 and 100 meV are indeed quasielliptic in all three models, and they remain closed curves for 150, 200, and 250 meV in the Drude and the semiclassical models, whereas the three outer curves in the optical model are open and clearly hyperbolic-shaped for 150, 200, and 250 meV (see
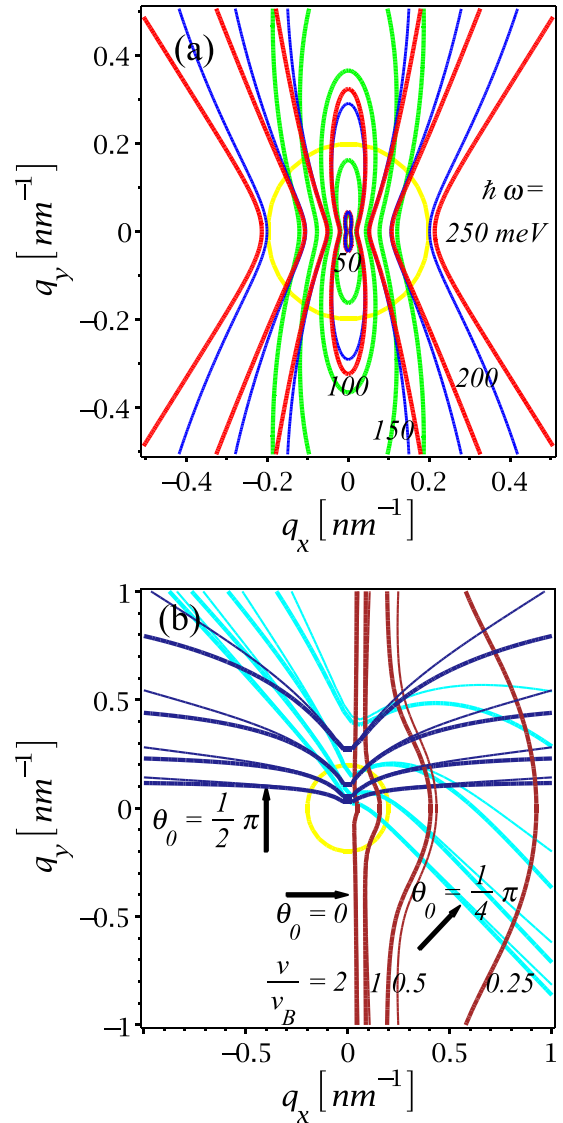
FIG. 1. (a) Isofrequency dispersion curves $\hbar\omega_p(q_x, q_y) = 50, 100, 150, 200$. and 250 meV for plasmon modes in freestanding phosphorene using: Drude model (green curves), optical model (red curves), and semiclassical model (blue curves). (b) Curves defined by $\omega_p(q_x, q_y) = v(q_x \cos\theta_0 + q_y \sin\theta_0)$ enforcing kinematic resonance for a particle moving above freestanding phosphorene using optical model (thick curves) and semiclassical model (thin curves) for the direction angles: $\theta_0 = 0$ (AC direction, brown curves), $\theta_0 = \pi/4$ (intermediate direction, cyan curves), and $\theta_0 = \pi/2$ (ZZ direction, navy curves), at the reduced speeds $\bar{v} = v/v_B = 0.25, 0.5, 1$, and 2 (the curves with $\bar{v} = 2$ pass the closest to the coordinate origin for all three directions). Also shown is the circle $q = 1/(2z_0)$ with $z_0 = 2.5$ nm (yellow curve).

Fig. S9 in Ref. [70]). We also show in Fig. 1(b) a circle $q = 1/(2z_0)$ with $z_0 = 2.5$ nm, enclosing a region of the (q_x, q_y) plane that makes a dominant contribution to the integrals in Eqs. (19) and (20), as implied by the exponential factor $\exp(-2qz_0)$ in them. One notices that the dispersion curves from the optical and semiclassical models are close inside that circle for all frequencies, whereas the Drude model only agrees with them for the curve with $\hbar\omega = 50$ meV.

Finally, notice that curves corresponding to different frequencies do not intersect each other within either model shown in Fig. 1(a).

We next discuss the directionality effects that may arise in the force components in Eqs. (19)–(21) due to anisotropic plasmon dispersions in a freestanding, doped phosphorene. Note that the integrands in Eqs. (19) and (20) involve a factor $\Im[1/\epsilon_{2D}(q_x, q_y, \omega)]$ related to the energy loss function of the system, which is strongly peaked at $\omega = \omega_p(q_x, q_y)$, when losses are negligible. At the same time, the kinematic resonance enforces the substitution $\omega = \mathbf{q} \cdot \mathbf{v}$ in the dielectric permittivity $\epsilon_{2D}(q_x, q_y, \omega)$ in those integrands. Therefore the main contribution to the integrals defining the longitudinal and transverse stopping forces comes from a curve in the (q_x, q_y) plane defined by the relation $\omega_p(q_x, q_y) = v(q_x \cos\theta_0 + q_y \sin\theta_0)$, where θ_0 is the direction angle of the moving charged particle. We show in Fig. 1(b) three sets of such curves for $\theta_0 = 0$ (AC direction, brown curves), $\theta_0 = \pi/4$ (an intermediate direction, cyan curves) and $\theta_0 = \pi/2$ (ZZ direction, navy curves), with each set consisting of four curves for the reduced speeds of $\bar{v} = 0.25, 0.5, 1$ and 2. [In each set, the curve with the highest speed of $\bar{v} = 2$ passes closest to the origin of the (q_x, q_y) plane. The curve with $\bar{v} = 0.25$ for $\theta_0 = 0$ in the semiclassical model lies outside the range of the (q_x, q_y) values shown in Fig. 1(b).] The thick lines show the results from the optical model, while the thin lines with same coloring show the corresponding results from the semiclassical model. All those curves exhibit a rich variety of shapes with, e.g., curves for the AC direction bending away from the origin, and the curves for the ZZ direction bending toward the origin. Obviously, there is a strong interplay of the parameters θ_0, v, and z_0, which define the external particle's trajectory, when it comes to sampling different plasmon dispersion relations of phosphorene. As in Fig. 1(a), we also show the same yellow circle in Fig. 1(b) as the bound of a domain of small wave numbers that are of interest for the particle distances selected in our study. Regarding the directionality effects in the case of image force, the integral in Eq. (21) involves a factor $\Re[1/\epsilon_{2D}(q_x, q_y, \omega) - 1]$, which is a Kramers-Kronig transform of the energy loss function of the system, and hence it can rapidly change its sign in the regions close to the isofrequency dispersion curves. [59] Accordingly, while the longitudinal and transverse stopping forces are expected to be strictly negative because $\Im[1/\epsilon_{2D}(q_x, q_y, \omega)] < 0$, it is not *a priori* obvious that the image force will always be attractive for an anisotropic 2D material, in contrast to the case of an isotropic 2D material, where the image force is necessarily attractive. [59]

Next, we study the effects of plasmon-phonon hybridization between the doped phosphorene and the SiO$_2$ substrate a distance $d = 0.4$ nm underneath it. In Fig. 2(a), we show the isofrequency curves for the dispersion surfaces obtained in the optical model (red curves) and semiclassical model (blue curves) for the same set of ω values as in Fig. 1(a). One may confirm that the two models are close to each other for the wave numbers $q \lesssim 0.2$ nm^{-1}, as was observed in Fig. 1. Using the same set of frequencies, we also show in Fig. 2(a) the isofrequency lines (yellow lines with a black arrow showing the direction of increasing frequency) for the
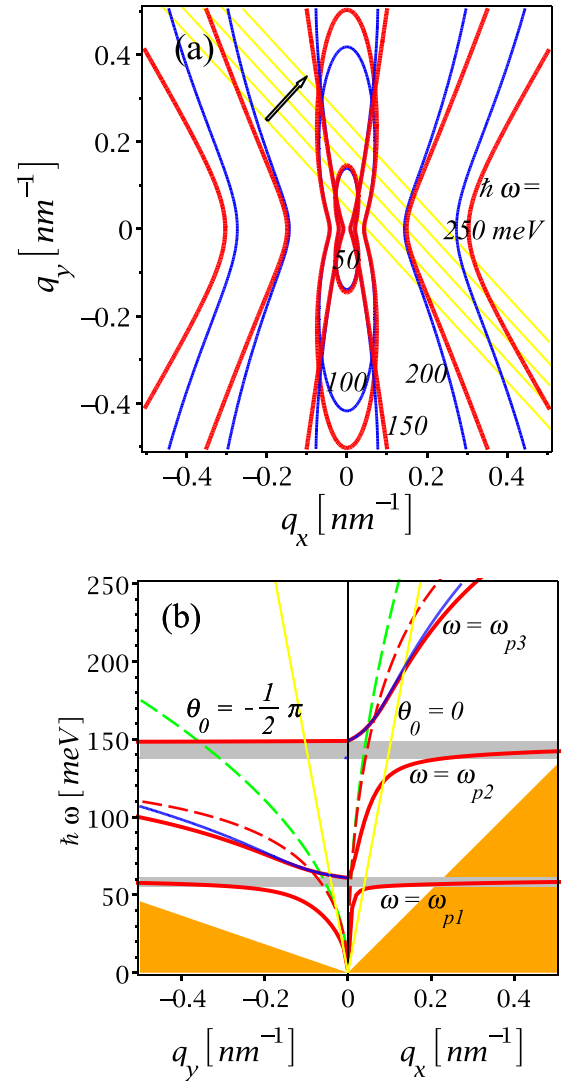
FIG. 2. (a) Isofrequency dispersion curves with $\hbar\omega = 50, 100, 150, 200,$ and 250 meV for plasmon-phonon modes in phosphorene supported by a SiO$_2$ substrate using optical model (red curves) and semiclassical model (blue curves), and the corresponding isofrequency lines for the plane $\omega = v_B(q_x \cos\theta_0 + q_y \sin\theta_0)$ with $\theta_0 = \pi/4$ (yellow lines). (b) Cross sections with the planes $q_x = 0$ (left side, $q_y < 0$) and $q_y = 0$ (right side, $q_x > 0$) are shown for dispersion surfaces of three plasmon-phonon modes, $\omega = \omega_{pk}(q_x, q_y)$ with $k = 1, 2,$ and 3 in phosphorene supported by SiO$_2$ using optical model (solid red curves) and semiclassical model (solid blue curves), and for the dispersion $\omega = \omega_p(q_x, q_y)$ in free phosphorene using Drude model (dashed green curves) and optical model (dashed red curves). The two grey shaded regions are the Reststrahlen bands of the SiO$_2$ substrate, while the two orange shaded areas are the electron-hole intraband continuum in phosphorene. Yellow lines show the cross sections for the plane $\omega = v_B(q_x \cos\theta_0 + q_y \sin\theta_0)$ with $\theta_0 = 0$ and $\theta_0 = -\pi/2$.

plane $\omega = v(q_x \cos\theta_0 + q_y \sin\theta_0)$, which enforces the kinematic resonance for a particle moving at the speed $v = v_B$ with the direction angle $\theta_0 = \pi/4$. Those lines confirm that the nonlocal effects are expected to be negligible when compared to the optical model for supported phosphorene in the

THz-MIR range by choosing large distances, $z_0 \gtrsim 1$ nm, and high particle speeds, $v \gtrsim v_B$.

It is remarkable in Fig. 2(a) that the curves with $\hbar\omega = 50$ and 100 meV intersect the curve with 150 meV for both models in the presence of the substrate, which does not happen in the case of a freestanding phosphorene in Fig. 1(a). This may be explained by the fact there are three separate sheets of the dispersion surfaces for hybrid plasmon-phonon modes, $\omega = \omega_{pk}(q_x, q_y)$ with $k = 1, 2, 3$, which exhibit avoided crossings over the entire (q_x, q_y) plane [76]. (See Fig. S1 in Ref. [70]). To elaborate on this, we show in Fig. 2(b) the cross sections of those three surfaces for the optical model (red curves) and the semiclassical model (blue curves) with the $q_x = 0$ plane (left side of that panel) and with the $q_y = 0$ plane (right side of the panel). Those cross-sections are labeled by $k = 1$ for the lowest, $k = 2$ for the middle, and $k = 3$ for the highest-lying dispersion frequencies of hybrid plasmon-phonon modes. The two horizontal gray shaded areas represent the Reststrahlen bands of the SiO_2 substrate. One notices that, in the optical model, the curve from $\omega_{p1}(q_x, q_y)$ starts at zero and gradually enters the lower-lying Reststrahlen band as both $|q_x|$ and $|q_y|$ increase, the curve from $\omega_{p2}(q_x, q_y)$ starts at ω_{SO1}, gradually enters the higher-lying Reststrahlen band as $|q_x|$ increases, and very slowly increases toward that band when $|q_y|$ increases, whereas the curve from $\omega_{p3}(q_x, q_y)$ starts at ω_{SO2}, increases with increasing $|q_x|$, but stays (almost) constant on the top of the higher-lying Reststrahlen band as $|q_y|$ increases. Also shown in Fig. 2(b) are the regions with a continuum of the intraband e-h excitations (orange shaded triangles). The proximity of those regions to the plasmon dispersion curves is the main cause of nonlocal effects in the semiclassical model of a freestanding phosphorene (see Sec.s S2 and S3 in Ref. [70]). The dispersion curves of the hybrid modes from the semiclassical model for a supported phosphorene are found to be indistinguishable from those from the optical model in Fig. 2(b), except in the cases (emphasized by blue lines) of the middle dispersion $\omega_{p2}(q_x, q_y)$ on the left side of the panel and the highest dispersion $\omega_{p3}(q_x, q_y)$ on the right side of the panel, where the phosphorene plasmon does not hybridize strongly with the substrate phonons. This indicates that the nonlocal effects in a supported phosphorene play a surprisingly negligible role in the regions of the (q_x, q_y, ω) space, which are characterized by strong plasmon-phonon hybridization.

For the sake of comparison, we also show in Fig. 2(b) the cross sections of the dispersion surfaces for a freestanding phosphorene, obtained from the optical model (dashed red curves) and from the Drude model (dashed green curves). One can see that the effects of the interband contribution are already substantial in the plasmon dispersion of a freestanding phosphorene as the wave numbers exceed $q \sim 0.1$ nm^{-1}. On the other hand, the dispersion curves from $\omega_{p2}(q_x, q_y)$ and $\omega_{p3}(q_x, q_y)$ in the presence of a substrate within the optical model tend to approach the corresponding curves in the case of freestanding phosphorene for increasing $|q_x|$ and $|q_y|$ values, respectively, i.e., in the regions characterized by a weak plasmon-phonon hybridization. Moreover, we show in Fig. 2(b) the cross sections (yellow lines) of the plane $\omega = v(q_x \cos\theta_0 + q_y \sin\theta_0)$, which enforces the kinematic resonance condition at the speed $v = v_B$ for two directions of

motion: $\theta_0 = 0$ (AC) and $\theta_0 = -\pi/2$ (ZZ). The intersections of those lines with the curves resulting from the dispersion relations imply dominant contributions of various plasmon excitation modes to the energy loss of the charge particle, which amount to the longitudinal stopping force. A qualitative analysis of Fig. 2(b) indicates that such intersections occur at generally higher plasmon energies when the motion takes place in the AC direction (right side of that panel) than in the ZZ direction (left side of that panel). This can be used to surmise that the magnitude of the force F_ℓ will be the largest when $\theta_0 = 0$.

B. Calculation of the force components

Having seen in the preceding section that the nonlocal effects are negligible for sufficiently small wave numbers, we use in this section our optical model for both the freestanding and supported phosphorene to show the dependence of all three force components, given in Eqs. (19)–(21), on the reduced speed $\bar{v} = v/v_B$ and the direction angle θ_0 for a charged particle moving at fixed distance of $z_0 = 50$ nm. A detailed comparison with the corresponding results for forces obtained using semiclassical model is given in Sec. S3 of Ref. [70]. All the forces are shown in a reduced form by normalizing them with $F_0 = (Ze)^2/(2z_0)^2$, the magnitude of the image force on a static point charge Ze a distance z_0 from the surface of an ideal conductor.

We note that, in Sec. S1 of Ref. [70], we provide a detailed discussion of those force components as functions of the distance and speed, while limiting our focus to the case of a freestanding phosphorene in order to assess the role of the interband contribution to the optical model and to emphasize the role of its anisotropy in comparison with a conductivity model for the related hypothetical isotropic 2D material (see Figs. S2– S8 in Ref. [70]).

In Fig. 3, we show the longitudinal stopping force, F_ℓ, which exhibits a typical dependence on speed, as seen in our previous work on isotropic 2D materials, represented by a supported graphene [59,63,76]. However, in the case of doped phosphorene, this force exhibits marked dependence on θ_0, especially near the speed $\bar{v} \sim 4$, where it reaches a prominent dip. The magnitude of that dip takes the largest value for motion along the AC direction ($\theta_0 = 0, \pi$), and the smallest value along the ZZ direction ($\theta_0 = \pi/2$). This can be rationalized by referring to conclusions drawn in Refs. [59,63,76] regarding the effects of increasing doping density n in graphene, which was found to generally give rise to an increase in magnitude of the stopping force. We recall that, in the present model of doped phosphorene, the strong inequality between the effective electron masses, $\bar{m}_x^* < \bar{m}_y^*$, stems from the effective number of charge carriers in the AC direction being much larger than in the ZZ direction, $n_x^e > n_y^e$ [32]. Drawing on the experience with graphene, one may then envision that a charged particle moving in the AC direction above phosphorene will interact with a higher effective number of charge carriers than in the case of motion in the ZZ direction, so that the corresponding F_ℓ will have a larger magnitude in the AC direction than in the ZZ direction. The ratio of those two values is quite large, about 2.3 [see Fig. 6(a) below]. In the presence of the substrate, the overall magnitude of the
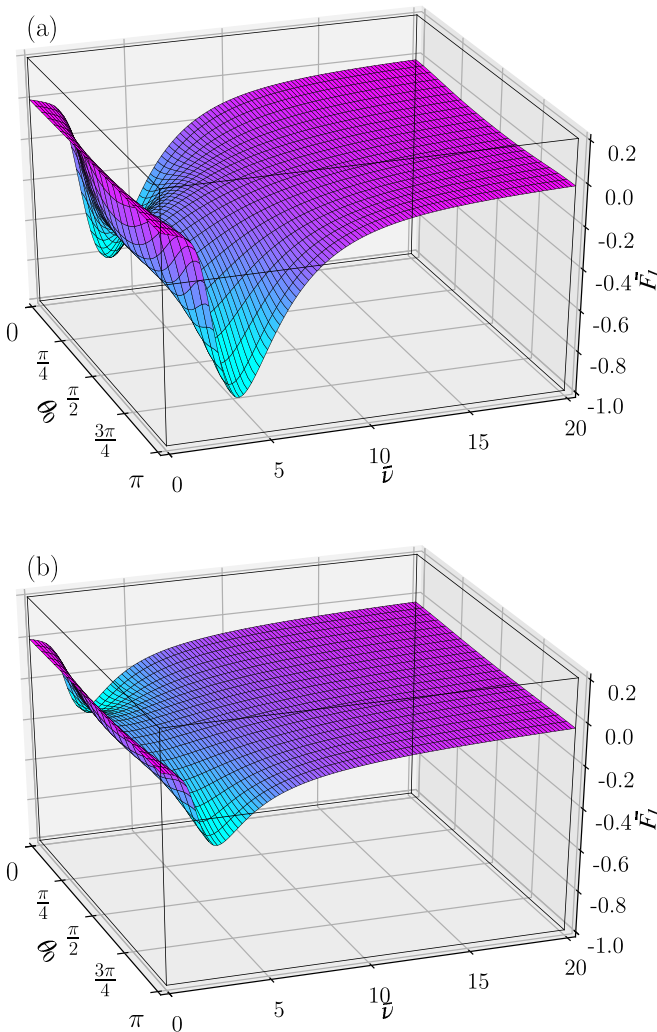
FIG. 3. Normalized longitudinal stopping force $\overline{F}_\ell = F_\ell/F_0$ vs normalized speed $\overline{v} = v/v_B$ and the direction angle θ_0 for a particle moving a distance $z_0 = 50$ nm above: (a) free phosphorene and (b) phosphorene supported by a SiO$_2$ substrate.

FIG. 4. Normalized transverse stopping force $\overline{F}_t = F_t/F_0$ vs normalized speed $\overline{v} = v/v_B$ and the direction angle θ_0 for a particle moving a distance $z_0 = 50$ nm above: (a) free phosphorene and (b) phosphorene supported by a SiO$_2$ substrate.

longitudinal stopping force is substantially reduced in comparison to the freestanding phosphorene, but the anisotropy is still quite prominent in the region of the main dip, with the ratio of magnitudes in the AC direction vs the ZZ direction being reduced to about 1.7. In the region of higher speeds, say, $\overline{v} \gtrsim 10$, the anisotropy effects in F_ℓ are drastically reduced, both for freestanding and supported phosphorene.

In Fig. 4, we show the transverse stopping force, F_t, which is generally zero above isotropic surfaces, but in the present case, it exhibits, quite dramatically, the effects of anisotropy both for freestanding and supported phosphorene. One can notice that F_t is an odd (antisymmetric) function of θ_0 with respect to the values $\theta_0 = 0, \pi$ (AC direction) and $\theta_0 = \pi/2$ (ZZ direction). Accordingly, F_t vanishes when the particle moves exactly along the AC and ZZ directions at any speed, and it reaches minimum/maximum values with opposite signs when it moves along intermediate directions. One sees that its dependence on speed for intermediate directions exhibits two local peaks at the speeds $\overline{v} \sim 2$ and $\overline{v} \sim 7$, which have the character of a minimum/maximim pair for directions

$0 < \theta_0 < \pi/2$ and a maximum/minimum pair for directions $\pi/2 < \theta_0 < \pi$ [see Fig. 6(b) below]. Considering the sign of F_t in those angular intervals, one may then claim that the transverse stopping force at a particle moving in an intermediate direction at the speed $\overline{v} \sim 2$ is directed toward the AC direction, whereas the force at the speed $\overline{v} \sim 7$ is directed toward the ZZ direction. The magnitude of F_t in the regions near those peaks is quite large and, in fact, comparable to the magnitude of the longitudinal stopping force F_ℓ, and it should be therefore observable in HREELS experiments upon rotation of the target about the z axis. As with F_ℓ, the overall magnitude of F_t is reduced in the presence of the substrate but, unlike F_ℓ, the effects of anisotropy in F_t persist, even when the speed exceeds $\overline{v} \sim 10$. It should be stressed that F_t exhibits a change of sign whenever it passes from one to another extremal point, seen in its dependence on both θ_0 and $\overline{v}$ in Fig. 4. In Ref. [70], we demonstrate that the dependence of F_t on distance z_0 also exhibits a maximum/minimum pair of points where it changes its sign (see Fig. S7(a) in Ref. [70]). Therefore the transverse stopping force exhibits a rich variety
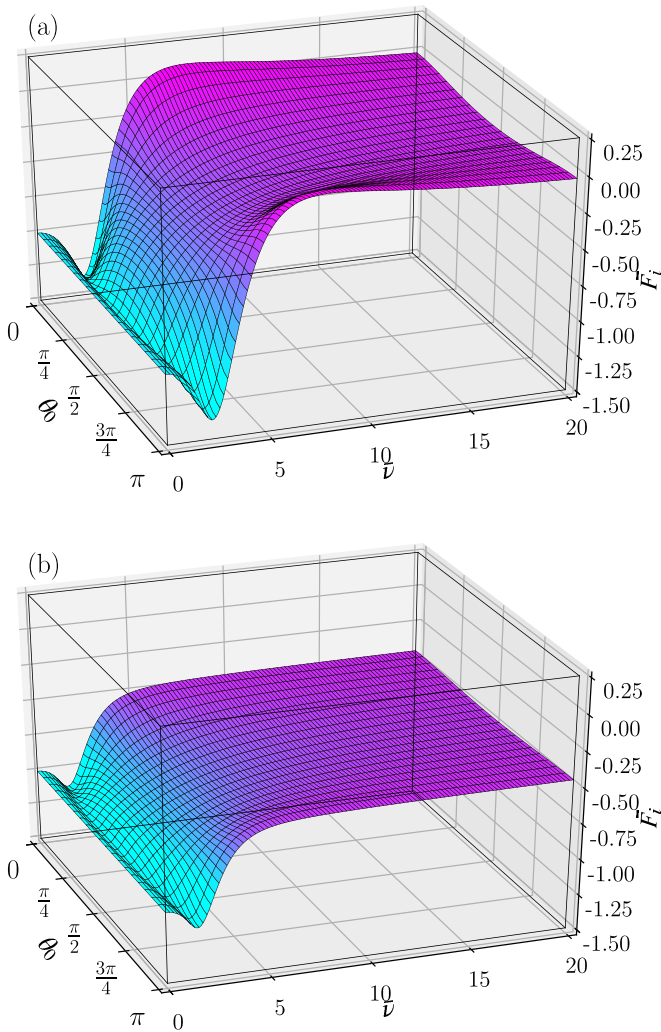
FIG. 5. Normalized image force $\overline{F}_i = F_i/F_0$ vs normalized speed $\overline{v} = v/v_B$ and the direction angle θ_0 for a particle moving a distance $z_0 = 50$ nm above: (a) free phosphorene and (b) phosphorene supported by a SiO₂ substrate.

of anisotropy effects when the direction angle θ_0, speed v *and* distance z_0 of the external charged particle are varied.

In Fig. 5, we show the image force, F_i, for freestanding and supported phosphorene. One may claim that its dependence on speed for most directions of motion is typical, as seen for dynamic image force above an isotropic 2D material [59,63,76], i.e., F_i starts from a finite value at $v = 0$ (which gives $F_i = -F_0$ owing to our use of the Drude model), goes through a prominent dip at $\overline{v} \sim 2$, and gradually approaches a constant value for $\overline{v} \gg 1$. However, as in the case of the longitudinal stopping force F_ℓ, image force exhibits large anisotropy, especially in a region of speeds near the dip, where the magnitude of F_i takes the largest value for motion along the AC direction ($\theta_0 = 0, \pi$), and the smallest value along the ZZ direction ($\theta_0 = \pi/2$), the ratio of the two values being about 1.7 [see Fig. 6(c) below]. This can be explained in a similar manner as for F_ℓ in terms of the effective number of charge carriers being higher in the AC direction than in the ZZ direction. As with F_ℓ, the presence of the substrate reduces the
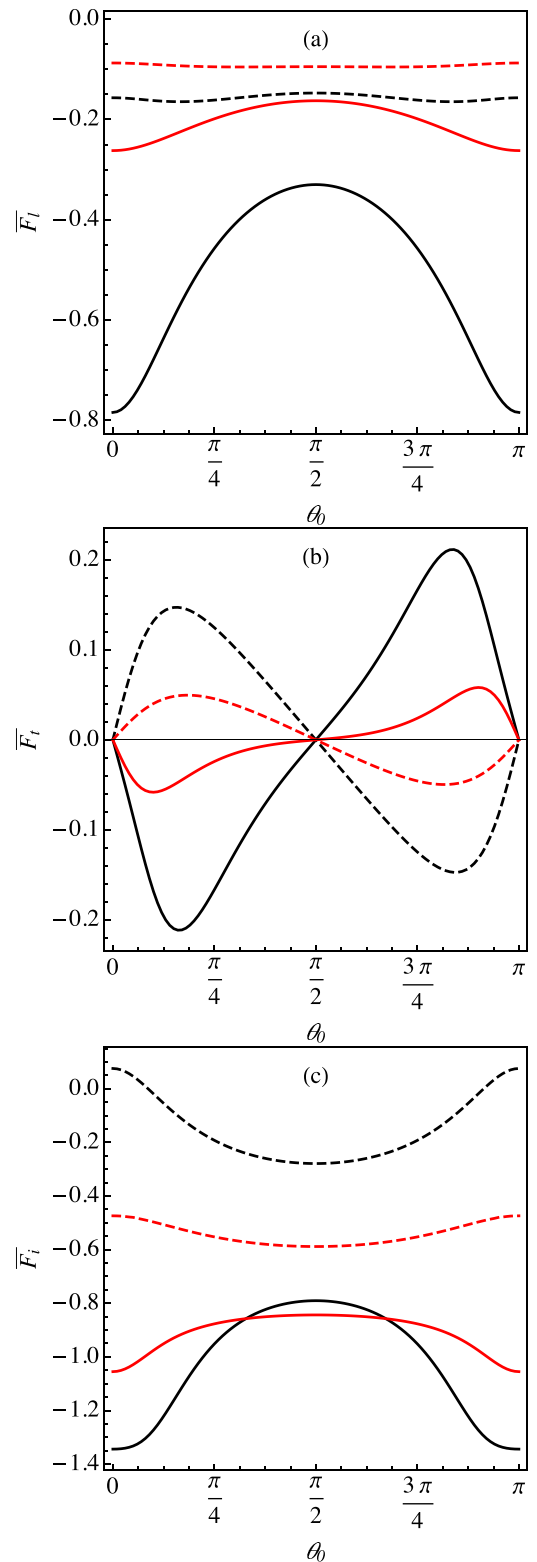
FIG. 6. Normalized forces vs the direction angle θ_0 for a particle moving a distance $z_0 = 50$ nm above free phosphorene (black curves) and phosphorene supported by a SiO₂ substrate (red curves) at the normalized speeds: $\overline{v} = 4$ (solid lines) and 9 (dashed lines) for the longitudinal stopping force $\overline{F}_\ell$ (a), and $\overline{v} = 2$ (solid lines) and 7 (dashed lines) for the transverse stopping force $\overline{F}_t$ (b) and the image force $\overline{F}_i$ (c).

magnitude of the image force in a broad region of speeds near the dip, and it also reduces the effects of anisotropy, bringing the ratio of the magnitudes in the AC and ZZ directions near the dip region down to about 1.3.

As regards the values of the image force when $\bar{v} \gg 1$, one sees that $F_i \to 0$ in Fig. 5(a), whereas $F_i \approx -0.5 \times F_0$ in Fig. 5(b), while still exhibiting some residual angular dependence due to anisotropy. As discussed elsewhere, [59] those limiting values can be assessed by using the infinite-frequency limit of the effective dielectric permittivity in Eq. (21). However, the most striking effect of our optical model is that the dynamic image force above freestanding phosphorene goes through a broad maximum where it becomes positive, i.e., it becomes repulsive for a particle moving in a direction close to the AC direction at a speed in the interval $5.7 \lesssim \bar{v} \lesssim 16.5$. This is not the case in the presence of the substrate, where the image force levels off at a value $\sim -0.5 \times F_0$ for speeds $\bar{v} \gtrsim 6$, while still exhibiting some angular dependence. The surprising reversal of the nature of the dynamic image force for freestanding phosphorene cannot be easily rationalized in view of the fact that the image force above an isotropic surface is necessarily negative (attractive), which can be rigorously proved by expressing the factor $\Re[1/\epsilon_{2D}(\mathbf{q}, \omega) - 1]$ in Eq. (21) in terms of the energy loss function $\Im[-1/\epsilon_{2D}(\mathbf{q}, \omega)] > 0$ by means of a Kramers-Kronig relation [59].

In Fig. 6, we show the cross sections of the surfaces displayed in Figs. 3–5 for fixed speeds, which are chosen to roughly lie in regions of the most prominent angular dependencies of all three forces for freestanding phosphorene. In particular, for the longitudinal stopping force shown in Fig. 6(a), we choose $\bar{v} = 4$ corresponding to the dip region and $\bar{v} = 9$, where F_ℓ begins to level off. For the transverse stopping force shown in Fig. 6(b), we choose $\bar{v} = 2$ and $\bar{v} = 7$, where F_t exhibits local extremal points. Lastly, for the image force shown in Fig. 6(c), we choose $\bar{v} = 2$ where F_i exhibits a dip and $\bar{v} = 7$, which corresponds to the broad maximum seen in the interval of positive F_i values in Fig. 5(a). A comparison of the curves for freestanding phosphorene (black curves) with those for supported phosphorene (red curves) confirms the previously noted effects of the substrate in reducing the overall magnitude of the forces and attenuating the signatures of anisotropy in their angular dependencies. In particular, one can see in Fig. 6(c) that the angular dependence of F_i at the speed $\bar{v} = 2$ exhibits maximum and minimum values in the AC and ZZ directions, respectively, for both freestanding and supported phosphorene. That angular dependence is reversed at the speed $\bar{v} = 7$, where the image forces goes through a range of positive values in an interval of angles $|\theta_0| \lesssim \pi/12$ about the AC direction ($\theta_0 = 0$) for freestanding phosphorene, but is reduced to a weak oscillation about the value $\sim -0.5 \times F_0$ in the case of supported phosphorene. On the other hand, it is gratifying to see in Fig. 6(b) that the transverse stopping force is still strong in the presence of the substrate and that it retains the peculiar antisymmetric features observed in its angular dependence with respect to the principal directions in the case of freestanding phosphorene.

Finally, we explore the role of anisotropy in the occurrence of positive values of the dynamic image force above freestanding phosphorene for incidence angles near the AC

(a)

(b)
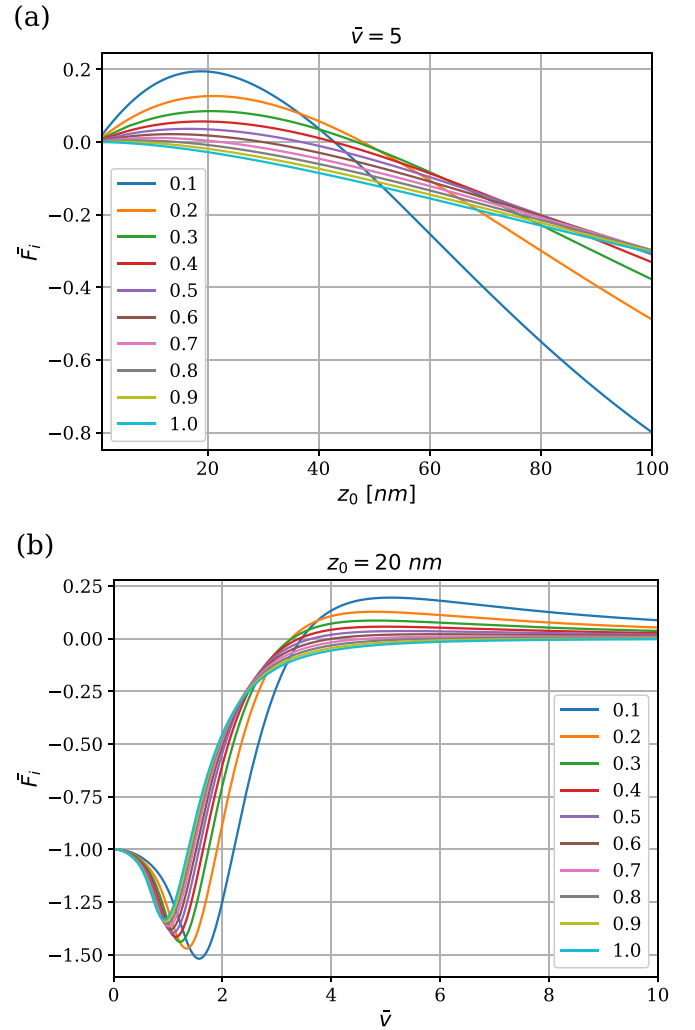
FIG. 7. Normalized image force $\overline{F}_i = F_i/F_0$ as a function of (a) the distance z_0 (in nm) for fixed normalized speed $\bar{v} = v/v_B = 5$ and (b) the normalized speed $\bar{v}$ for fixed distance $z_0 = 20$ nm. Results are shown for a Drude model of doped phosphorene with $n = 10^{13}$ cm^{-2} where the product of the reduced electron masses is kept fixed at $\overline{m}_x^* \overline{m}_y^* = 0.149$, while their ratio $R = \overline{m}_x^*/\overline{m}_y^*$ is varied in an interval from $R = 0.1$ to $R = 1$ in steps of 0.1.

direction. As discussed in Figs. S2 and S3 of Ref. [70], it appears that, for $\theta_0 = 0$, the anisotropy in the adopted Drude model is responsible for the image force becoming positive when a combination of the speed and distance, given by v^2/z_0, exceeds a fixed value for the parameters used in this section. To further explore this anisotropy, we show in Fig. 7 the reduced image force for $\theta_0 = 0$ obtained from a Drude model, in which we keep the product of the reduced effective electron masses fixed at the value obtained from the *ab initio* data, $\overline{m}_x^* \overline{m}_y^* = 0.149$, while varying their ratio $R = \overline{m}_x^*/\overline{m}_y^*$ in an interval from $R = 0.1$ (a very anisotropic case) to $R = 1$ (isotropic 2D material) in steps of 0.1. The results are shown in Fig. 7(a) as a function of distance for the normalized speed fixed at $\bar{v} = 5$, and in Fig. 7(b) as a function of speed $\bar{v}$ for the distance fixed at $z_0 = 20$ nm. One can see that even a small deviation from the isotropic case causes the image force to take positive values for distances $z_0 < z_c$ at fixed $\bar{v}$

and for speeds $\overline{v} > \overline{v}_c$ at fixed z_0, with the critical values z_c and $\overline{v}_c$ being both dependent on the ratio of masses, R, in a nonmonotonous manner. However, as shown in Figs. S2 and S3 of Ref. [70], the inclusion of the interband contribution into the optical model counteracts the Drude contribution and lowers the image force values. In some cases of lower speeds and shorter distances, the optical model (as well as the semiclassical model) yields negative values of the image force, while in other cases those values remain positive. Because the domain of integration in Eq. (21) for the image force implies the occurrence of large frequencies, it is conceivable that taking a full contribution from the interband electron transition over a broad range of frequencies may take over the anisotropic Drude model and render the image force negative in a full range of the particle-related parameters: θ_0, v, and z_0.

IV. CONCLUDING REMARKS

We have presented a simple analytical model for anisotropic optical conductivity of doped phosphorene, which is suitable for the THz-MIR frequency range, with parameters deduced from *ab initio* calculations. A novel feature of the model is the inclusion of a contribution from high-energy interband electronic transitions in the static limit, which in coaction with the anisotropic Drude model for intraband transitions, enables a topological transition of the isofrequency dispersion curves for plasmon modes in doped phosphorene from quasielliptic (occurring at the THz) to hyperbolic (occurring at the MIR). Besides applications to freestanding phosphorene, this model was paired with a simple dielectric function describing optical phonons in a SiO$_2$ substrate, enabling us to explore plasmon-phonon hybridization taking place in a supported phosphorene. As expected, the dispersion surface is split into three sheets corresponding to three hybrid modes separated by two Reststrahlen bands of frequencies in the SiO$_2$ substrate. This hybridization preserves the elliptic and hyperbolic characters of isofrequency curves in the frequency ranges imposed by the conductivity model of phosphorene, while enabling pairs of curves with different character to intersect in the plane of the wave-vector components.

The above dielectric description of the target system was further used to calculate the force acting on a classical point charge moving parallel to phosphorene at a distance of $z_0 = 50$ nm and with speeds of relevance to the HREELS under oblique incidence or to grazing scattering of ions. This scattering geometry is particularly sensitive to any anisotropy of the target surface, and we have indeed observed substantial quantitative effects of phosphorene's anisotropy in the components of that force, which are all strongly affected by changing the speed and the direction of motion of the incident charged particle. In addition to the quantitative effects, there are some striking qualitative outcomes of the anisotropy. First, besides the longitudinal stopping force, which acts to slow down the incident particle, there exists a transverse stopping force, which is a dissipative force that acts parallel to the surface but perpendicular to the particle's trajectory. This force is quite strong and is, in fact, comparable to the longitudinal stopping force, and it rapidly changes its character as both the speed and the direction of motion are varied. For example, when the

particle moves in a direction that is not oriented along phosphorene's principal directions, the transverse stopping force bends the trajectory of that particle toward the AC direction when its speed (normalized by the Bohr speed, $\overline{v} = v/v_B$) is $\overline{v} \sim 2$, but it reverses the character as the speed increases, and bends the trajectory toward the ZZ direction when the speed is $\overline{v} \sim 7$. Finally, the dynamical image force on the incident charged particle is a conservative force that should normally attract the particle toward the target surface, which was also observed to exhibit substantial quantitative effects of the anisotropy of phosphorene. However, the image force undergoes a surprising qualitative change by reversing its sign and becoming a repulsive force when the particle moves above freestanding phosphorene in a direction close to the AC direction with the speed that falls in an interval $6 \lesssim \overline{v} \lesssim 16$. This implausible result may be traced to a dominant role played by the anisotropic Drude model at high frequencies, which warrants further investigation. We have shown that this shortcoming of the anisotropic Drude model could be partially remedied by including a low-frequency correction to the conductivity due to the interband electron transitions in phosphorene. This observation offers a promising route to further explore the change of sign in the dynamic image force, which will be taken up in future work by using *ab-initio* data for the in-plane conductivity in doped phosphorene over a broad range of frequencies. [32] Similar counterintuitive manifestations of a repulsive dynamic image force were discovered by using relativistic treatment of the particle beam interactions with targets in configurations that differ from ours [62,79]. Accordingly, it is possible that a relativistic treatment of the image force [80–82] can shed more light on its behavior at high particle speeds in the present context, which will also be taken up in future work.

The main effects of the SiO$_2$ substrate were found to reduce the magnitude of all the force components in the regions of speeds where they exhibit extremal values and to reduce the relative amount of anisotropy as manifested in their dependence on the direction of motion. The image force above supported phosphorene approaches a finite value with little angular dependence as the speed increases beyond $\overline{v} \approx 6$, which eliminates the region where the image force exhibits repulsive character in the case of freestanding phosphorene. Nevertheless, the transverse stopping force retains a large magnitude and still exhibits strong anisotropy in the presence of a substrate, which may be observable in carefully designed HREELS experiments using a reflection of ∼100 eV electrons under grazing incidence. To be able to model such experiments, one would require expressions for the force components that are valid for all particle distances, including the situation when the particle interacts strongly with the bulk modes in the substrate. It was shown that the use of a bulk dielectric function for a polar substrate suffices for capturing all the essential features of its phonon spectra in HREELS using near-specular reflection under grazing incidence when the substrate thickness exceeds 2–3 nm [41,42]. A more severe limitation for possible modeling applications of our theory is the restriction to large distances, which is used in this article only to facilitate our derivation of a simple conductivity model for phosphorene by invoking its optical limit. In that respect, we shall take in future work a full account of the nonlocal

effects by using the momentum-dependent *ab initio* data for phosphorene's conductivity [32] to numerically compute the force components at a full range of particle distances from phosphorene. Only then would it become feasible to simulate realistic trajectories of the incident particles, and accordingly asses the role of anisotropy in the reflected electron spectra. One possible way to perform this task is to use a Monte Carlo type of simulation based on classical equations for the electron trajectory under grazing incidence upon phosphorene, [83] which will be augmented by a velocity– and distance-dependent anisotropic in-plane friction force, while the motion in the perpendicular direction will be treated as adiabatic [48,83].

[1] B. Li, C. Lai, G. Zeng, D. Huang, L. Qin, M. Zhang, M. Cheng, X. Liu, H. Yi, C. Zhou, F. Huang, S. Liu, and Y. Fu, Small **15**, 1804565 (2019).

[2] F. Xia, H. Wang, and Y. Jia, Nat. Commun. **5**, 4458 (2014).

[3] L. Li, Y. Yu, G. J. Ye, Q. Ge, X. Ou, H. Wu, D. Feng, X. H. Chen, and Y. Zhang, Nat. Nanotechnol. **9**, 372 (2014).

[4] H. Liu, A. T. Neal, Z. Zhu, Z. Luo, X. Xu, D. Tománek, and P. D. Ye, ACS Nano **8**, 4033 (2014).

[5] X. Wang and S. Lan, Adv. Opt. Photon. **8**, 618 (2016).

[6] W. Ma, P. Alonso-Gonzalez, S. Li, A. Y. Nikitin, J. Yuan, J. Martin-Sanchez, J. Taboada-Gutierrez, I. Amenabar, P. Li, S. Velez, C. Tollan, Z. Dai, Y. Zhang, S. Sriram, K. Kalantar-Zadeh, S.-T. Lee, R. Hillenbrand, and Q. Bao, Nature (London) **562**, 557 (2018).

[7] X. Chen, J. S. Ponraj, D. Fan, and H. Zhang, Nanoscale **12**, 3513 (2020).

[8] H. Liu, A. T. Neal, M. Si, Y. Du, and P. D. Ye, EEE Electron Device Lett. **35**, 795 (2014).

[9] C. Wang, G. Zhang, S. Huang, Y. Xie, and H. Yan, Adv. Opt. Mater. **8**, 1900996 (2020).

[10] Z. Dai, G. Hu, Q. Ou, L. Zhang, F. Xia, F. J. Garcia-Vidal, C.-W. Qiu, and Q. Bao, Chem. Rev. **120**, 6197 (2020).

[11] J. S. Gomez-Diaz and A. Alú, ACS Photonics **3**, 2211 (2016).

[12] B. Deng, R. Frisenda, C. Li, X. Chen, A. Castellanos-Gomez, and F. Xia, Adv. Opt. Mater. **6**, 1800365 (2018).

[13] J. Miao, L. Zhang, and C. Wang, 2D Mater. **6**, 032003 (2019).

[14] T. Low, A. S. Rodin, A. Carvalho, Y. Jiang, H. Wang, F. Xia, and A. H. Castro Neto, Phys. Rev. B **90**, 075434 (2014).

[15] T. Low, R. Roldán, H. Wang, F. Xia, P. Avouris, L. M. Moreno, and F. Guinea, Phys. Rev. Lett. **113**, 106802 (2014).

[16] J. Kim, S. S. Baik, S. H. Ryu, Y. Sohn, S. Park, B.-G. Park, J. Denlinger, Y. Yi, H. J. Choi, and K. S. Kim, Science **349**, 723 (2015).

[17] D. T. Debu, S. J. Bauman, D. French, H. O. Churchill, and J. B. Herzog, Sci. Rep. **8**, 3224 (2018).

[18] E. van Veen, A. Nemilentsau, A. Kumar, R. Roldán, M. I. Katsnelson, T. Low, and S. Yuan, Phys. Rev. Appl. **12**, 014011 (2019).

[19] S. Biswas, W. S. Whitney, M. Y. Grajower, K. Watanabe, T. Taniguchi, H. A. Bechtel, G. R. Rossman, and H. A. Atwater, Sci. Adv. **7**, eabd4623 (2021).

[20] S. Biswas, M. Y. Grajower, K. Watanabe, T. Taniguchi, and H. A. Atwater, Science **374**, 448 (2021).

[21] J. S. Gomez-Diaz, M. Tymchenko, and A. Alù, Phys. Rev. Lett. **114**, 233901 (2015).

[22] D. Correas-Serrano, J. S. Gomez-Diaz, A. A. Melcon, and A. Alú, J. Opt. **18**, 104006 (2016).

[23] A. Nemilentsau, T. Low, and G. Hanson, Phys. Rev. Lett. **116**, 066804 (2016).

[24] Z. Su and Y. Wang, Nanomaterials **10**, 1694 (2020).

[25] S. A. Hassani Gangaraj, T. Low, A. Nemilentsau, and G. W. Hanson, IEEE Trans. Antennas Propag. **65**, 1174 (2017).

[26] A. Nemilentsau, T. Stauber, G. Gómez-Santos, M. Luskin, and T. Low, Phys. Rev. B **99**, 201405(R) (2019).

[27] H. Hajian, I. D. Rukhlenko, G. W. Hanson, T. Low, B. Butun, and E. Ozbay, Nanophotonics **9**, 3909 (2020).

[28] S. Xiao, T. Liu, L. Cheng, C. Zhou, X. Jiang, Z. Li, and C. Xu, J. Lightwave Technol. **37**, 3290 (2019).

[29] R. J. Wu, M. Topsakal, T. Low, M. C. Robbins, N. Haratipour, J. S. Jeong, R. M. Wentzcovitch, S. J. Koester, and K. A. Mkhoyan, J. Vac. Sci. Technol., A **33**, 060604 (2015).

[30] B. Ghosh, P. Kumar, A. Thakur, Y. S. Chauhan, S. Bhowmick, and A. Agarwal, Phys. Rev. B **96**, 035422 (2017).

[31] E. Gaufrés, F. Fossard, V. Gosselin, L. Sponza, F. Ducastelle, Z. Li, S. G. Louie, R. Martel, M. Côté, and A. Loiseau, Nano Lett. **19**, 8303 (2019).

[32] D. Novko, K. Lyon, D. J. Mowbray, and V. Despoja, Phys. Rev. B **104**, 115421 (2021).

[33] F. J. García de Abajo, Rev. Mod. Phys. **82**, 209 (2010).

[34] A. Polman, M. Kociak, and F. J. García de Abajo, Nat. Mater. **18**, 1158 (2019).

[35] R. J. Warmack, R. S. Becker, V. E. Anderson, R. H. Ritchie, Y. T. Chu, J. Little, and T. L. Ferrell, Phys. Rev. B **29**, 4375 (1984).

[36] P. A. Crozier, Ultramicroscopy **180**, 104 (2017).

[37] F. S. Hage, R. J. Nicholls, J. R. Yates, D. G. McCulloch, T. C. Lovejoy, N. Dellby, O. L. Krivanek, K. Refson, and Q. M. Ramasse, Sci. Adv. **4**, eaar7495 (2018).

[38] O. L. Krivanek, N. Dellby, J. A. Hachtel, J.-C. Idrobo, M. T. Hotz, B. Plotkin-Swing, N. J. Bacon, A. L. Bleloch, G. J. Corbin, M. V. Hoffman, C. E. Meyer, and T. C. Lovejoy, Ultramicroscopy **203**, 60 (2019).

[39] H. Ibach and D. Mills, *Electron Energy Loss Spectroscopy and Surface Vibrations* (Academic, New York, 1982).

[40] P. Lambin, A. Lucas, and J. Vigneron, Surf. Sci. **182**, 567 (1987).

[41] P. Senet, P. Lambin, J.-P. Vigneron, and I. D. A. A. Lucas, Surf. Sci. **226**, 307 (1990).

[42] P. Lambin, P. Senet, and A. A. Lucas, Phys. Rev. B **44**, 6416 (1991).

[43] P. Lambin, L. Henrard, P. Thiry, C. Silien, and J. Vigneron, J. Electron Spectrosc. Relat. Phenom. **129**, 281 (2003).

[44] A. Politano and G. Chiarello, Nanoscale **6**, 10927 (2014).

[45] K. J. Snowdon, D. J. O'Connor, and R. J. MacDonald, Phys. Rev. Lett. **61**, 1760 (1988).

[46] H. Winter, J. Phys.: Condens. Matter **8**, 10149 (1996).

[47] A. G. Borisov, A. Mertens, H. Winter, and A. K. Kazansky, Phys. Rev. Lett. **83**, 5378 (1999).

[48] Y.-H. Song, Y.-N. Wang, and Z. L. Miskovic, Phys. Rev. A **63**, 052902 (2001).

[49] A. A. Lucas, M. Sunjic, and G. Benedek, J. Phys.: Condens. Matter **25**, 355009 (2013).

[50] B. Jin, H. Zhou, Z. Zong, X. Zhang, G. Wang, L. Zhou, and X. Chen, RSC Adv. **11**, 4489 (2021).

[51] Y. Liu, R. F. Willis, K. V. Emtsev, and T. Seyller, Phys. Rev. B **78**, 201403(R) (2008).

[52] J. Lu, K. P. Loh, H. Huang, W. Chen, and A. T. S. Wee, Phys. Rev. B **80**, 113410 (2009).

[53] Y. Liu and R. F. Willis, Phys. Rev. B **81**, 081406(R) (2010).

[54] K. F. Allison and Z. L. Miskovic, Nanotechnology **21**, 134017 (2010).

[55] R. J. Koch, T. Seyller, and J. A. Schaefer, Phys. Rev. B **82**, 201413(R) (2010).

[56] T. Langer, D. F. Forster, C. Busse, T. Michely, H. Pfnur, and C. Tegenkamp, New J. Phys. **13**, 053006 (2011).

[57] R. J. Koch, S. Fryska, M. Ostler, M. Endlich, F. Speck, T. Hänsel, J. A. Schaefer, and T. Seyller, Phys. Rev. Lett. **116**, 106802 (2016).

[58] K. Akbari, S. Segui, Z. L. Miskovic, J. L. Gervasoni, and N. R. Arista, Phys. Rev. B **98**, 195410 (2018).

[59] M. R. Preciado Rivas, M. Moshayedi, and Z. L. Miskovic, J. Appl. Phys. **130**, 173103 (2021).

[60] O. H. Crawford, Phys. Rev. A **42**, 1390 (1990).

[61] C. Maciel-Escudero, A. Konečná, R. Hillenbrand, and J. Aizpurua, Phys. Rev. B **102**, 115431 (2020).

[62] P. R. Ribic, Phys. Rev. Lett. **109**, 244801 (2012).

[63] K. F. Allison, D. Borka, I. Radovic, L. Hadzievski, and Z. L. Miskovic, Phys. Rev. B **80**, 195405 (2009).

[64] Z. L. Mišković, P. Sharma, and F. O. Goodman, Phys. Rev. B **86**, 115437 (2012).

[65] D. Novko, M. Šunjić, and V. Despoja, Phys. Rev. B **93**, 125413 (2016).

[66] V. A. Margulis and E. E. Muryumin, Phys. Rev. B **98**, 165305 (2018).

[67] A. M. Holmes and G. W. Hanson, J. Appl. Phys. **129**, 015302 (2021).

[68] V. Despoja, T. Djordjevic, L. Karbunar, I. Radovic, and Z. L. Miskovic, Phys. Rev. B **96**, 075433 (2017).

[69] M. N. Gjerding, L. S. R. Cavalcante, A. Chaves, and K. S. Thygesen, J. Phys. Chem. C **124**, 11609 (2020).

[70] See Supplemental Material at http://link.aps.org/supplemental/10.1103/PhysRevB.105.075429 for additional results and a derivation of the semiclassical model.

[71] P. L. Bhatnagar, E. P. Gross, and M. Krook, Phys. Rev. **94**, 511 (1954).

[72] N. D. Mermin, Phys. Rev. B **1**, 2362 (1970).

[73] I. Radovic, L. Hadzievski, and Z. L. Miskovic, Phys. Rev. B **77**, 075428 (2008).

[74] G. Lovat, G. W. Hanson, R. Araneo, and P. Burghignoli, Phys. Rev. B **87**, 115429 (2013).

[75] S. Ahn and S. Das Sarma, Phys. Rev. B **103**, L041303 (2021).

[76] T. Marinkovic, I. Radovic, D. Borka, and Z. L. Miskovic, Plasmonics **10**, 1741 (2015).

[77] A. Kumar, T. Low, K. H. Fung, P. Avouris, and N. X. Fang, Nano Lett. **15**, 3172 (2015).

[78] A. N. Rudenko, S. Brener, and M. I. Katsnelson, Phys. Rev. Lett. **116**, 246401 (2016).

[79] I. Carmeli, M. A. Itskovsky, Y. Kauffmann, Y. Shaked, S. Richter, T. Maniv, and H. Cohen, Phys. Rev. B **85**, 041405(R) (2012).

[80] A. Rivacoba and N. Zabala, New J. Phys. **16**, 073048 (2014).

[81] K. Akbari, Z. L. Miskovic, S. Segui, J. L. Gervasoni, and N. R. Arista, ACS Photonics **4**, 1980 (2017).

[82] Z. L. Miskovic, K. Akbari, S. Segui, J. L. Gervasoni, and N. R. Arista, Nucl. Instrum. Methods Phys. Res., Sect. B **422**, 18 (2018).

[83] D. Borka, S. Petrovic, N. Neskovic, D. J. Mowbray, and Z. L. Miskovic, Phys. Rev. A **73**, 062902 (2006).